Journal of Materials Chemistry

Cite this: J. Mater. Chem., 2012, 22, 4825

www.rsc.org/materials

PAPER

High thermoelectric figure-of-merit in p-type nanostructured $(Bi,Sb)_2Te_3$ fabricated *via* hydrothermal synthesis and evacuated-and-encapsulated sintering

Chia-Jyi Liu,* Hsin -Chang Lai, Yen-Liang Liu and Liang-Ru Chen

Received 13th October 2011, Accepted 24th December 2011
DOI: 10.1039/c2jm15185e

High ZT values of nanostructured $Bi_{2-x}Sb_xTe_3$ for energy conversion are fabricated by hydrothermal methods followed by cold-pressing and sintering in an evacuated and encapsulated ampoule. We show that the sample with a nominal composition of $x = 1.55$ exhibits a dimensionless figure of merit $ZT =$ 1.65 at 290 K and 1.75 at 270 K with significant 60–70% improvement of that of the commercial state-of-the-art Bi_2Te_3 materials around room temperature. The significant ZT improvement arises from the much-reduced thermal conductivity. The low thermal conductivity is mainly due to the increased phonon scattering in the nanostructured materials.

I. Introduction

Waste heat recovery and environmentally friendly refrigeration using thermoelectric materials have attracted considerable attention due to their potential for direct conversion of heat to electricity *via* the Seebeck effect and cooling capability *via* the Peltier effect without using coolants. It has been estimated that the waste heat recovery using efficient thermoelectric generator (TEG) in automotive industry would have hundreds of millions of gallons of fuel savings per year.[1] The power generation efficiency η_{TE} for a TEG is expressed as[2]

$$\eta_{TE} = \left(\frac{T_H - T_C}{T_H}\right)\left(\frac{\sqrt{1+ZT_M}-1}{\sqrt{1+ZT_M}+\frac{T_C}{T_H}}\right), \quad (1)$$

where $T_M = (T_H + T_C)/2$ is the mean temperature; T_H and T_C are the temperatures of heat source and heat sink, respectively. The figure of merit (Z) of thermoelectric materials is determined by three transport parameters and can be expressed as $Z = \sigma S^2/\kappa$, where σ, S, and κ are the electrical conductivity, thermopower, and thermal conductivity, respectively. The commercial bismuth alloys show the highest dimensionless figure of merit $ZT \approx 1$, where T is the absolute temperature, between room temperature and 100 °C. Since unexploited natural heat below 100 °C is abundant in our surroundings, the development of a high efficient thermoelectric material of bismuth alloys is essential for the practical use of waste heat recovery with TEG below 100 °C.

However, it is intrinsically difficult to develop a thermoelectric material that simultaneously has high electrical conductivity, large thermopower, and low thermal conductivity for maximizing ZT values. Because of the mutual dependencies among the electrical conductivity, thermopower, and thermal conductivity due to the Boltzmann transport equation, the high electrical conductivity would be accompanied by a small thermopower for materials with one type of charge carrier. The thermal conductivity of a solid is determined by both the electronic and lattice contributions, that is, $\kappa = \kappa_{el} + \kappa_L$, where κ_{el} and κ_L represent the electronic and lattice thermal conductivity, respectively. Assuming a common relaxation time exists for electrical and thermal processes, the Wiedemann–Franz law poses a constraint on the constant relationship between the electrical conductivity and thermal conductivity contributed from charge carriers at a given temperature. This would make it unable to pursue a higher figure of merit by maximizing the electrical conductivity while minimizing κ_{el}. Nevertheless, high efficient thermoelectric material can be obtained by reducing the lattice thermal conductivity *via* introducing the phonon-glass electron-crystal approach[2] or the bulk nanostructuring approach.[3]

In the bulk nanostructuring approach, the lattice thermal conductivity can be significantly reduced by interface phonon scattering mechanism due to an increased number of interfaces in the bulk material consisting of nanograins. This paradigm has been recently demonstrated in high efficient p-type bismuth antimony telluride alloys by several nanofabrication techniques. These techniques are ball milling followed by hot pressing,[4] melt spinning followed by spark plasma sintering,[5] and melt spinning followed by mixing micronsized with nanosized particles and hot pressing.[6]

The synthetic conditions of hydrothermal methods usually take place in a closed system at low temperatures. Several groups have reported synthesis of nanocrystals of Bi_2Te_3 and $Bi_{2-x}Sb_xTe_3$ using hydrothermal or solvothermal methods.[7–10]

Department of Physics, National Changhua University of Education, Changhua, 500, Taiwan. E-mail: liucj@cc.ncue.edu.tw

However, most of these reports focus on the synthesis without mentioning consolidating these nanocrystal powders for further thermoelectric property characterization. We have recently demonstrated that consolidating the $Bi_{0.5}Sb_{1.5}Te_3$ nanocrystal powders by cold pressing and sintering in an evacuated Pyrex ampoule is an easy and effective way to obtain a very low thermal conductivity of 0.37 W m^{-1} K with a dimensionless figure of merit $ZT = 0.93$ at 295 K.[11]

The electronic transport properties of the $Bi_{2-x}Sb_xTe_3$ can be tuned through carefully controlling the Sb content. Due to the high volatility of Te, both Sb and Bi tend to occupy the Te sublattice and form the anti-site defects, resulting in an acceptor role and hence p-type doping.[12] This can be viewed as a key feature of this system. Formation of anti-site defects can be described by the following equations:

$$Bi_2Te_3 \rightarrow 2Bi'_{Te} + 2V_{Bi} + Te_{Te} + 2\ Te_{(g)} + 2h, \quad (2)$$

$$Sb_2Te_3 \rightarrow 2Sb'_{Te} + 2V_{Sb} + Te_{Te} + 2\ Te_{(g)} + 2h, \quad (3)$$

where Bi'_{Te} and Sb'_{Te} are the anti-site defects, V_{Bi} and V_{Sb} are the vacancies, and h is the electron hole. At low x, the sign of charge carrier is negative for the ternary $Bi_{2-x}Sb_xTe_3$, and turns positive at high doping level of x.[13,14] The negative carrier concentration decreases with increasing x and changes sign above $x > 1$.

Here we report on the $Bi_{2-x}Sb_xTe_3$ fabricated using hydrothermal methods followed by sintering in an evacuated and encapsulated ampoule and show that the sample with a nominal composition of $x = 1.55$ exhibits high performance p-type thermoelectric properties. The $x = 1.55$ sample exhibits a higher hole concentration than that of $x = 1.5$, which results in an improved electrical conductivity and an increase of thermal conductivity for the former. When comparing the $x = 1.55$ sample with the $x = 1.5$ one, a 70% increase of dimensionless figure of merit arises from a twofold increase of electrical conductivity and a 13% increase of thermal conductivity. The $x = 1.55$ sample shows a state-of-the-art dimensionless figure of merit $ZT = 1.65$ at 290 K and 1.75 at 270 K with significant improvement of that of the commercial Bi_2Te_3 materials.[4]

2. Experimental

2.1 Preparation of $Bi_{2-x}Sb_xTe_3$ powders by hydrothermal methods

$Bi_{2-x}Sb_xTe_3$ ($x = 1.45$, 1.5, 1.55, and 1.56) powders were synthesized using hydrothermal methods. According to above nominal composition, Te powders, $BiCl_3$, $SbCl_3$, ethylenediaminetetraacetic acid (EDT, and deionized water were quantitatively added into a polytetrafluoroethylene (PTFE) cylindrical container and well stirred at room temperature for 1 h. KOH was then added to the above solution and stirred for 1 h, followed by adding $NaBH_4$ and stirring for another 0.5 h. The PTFE container containing the above solution was transferred to a pressure bomb and heated at 140 °C for 36 h in a box furnace. $NaBH_4$ is required to inhibit the formation of Bi_2O_3. The resulting powders were washed by deionized water and then absolute ethanol, followed by drying at 80 °C.

2.2. Consolidation of $Bi_{2-x}Sb_xTe_3$ powders

The $Bi_{2-x}Sb_xTe_3$ powders were cold pressed into parallelepiped using a uniaxial press. The resulting parallelepiped was then loaded into a Pyrex ampoule. The ampoule was evacuated using a diffusion pump to reach a vacuum of 10^{-5}–10^{-6} torr and then sealed. The parallelepiped in the encapsulated ampoule was then transferred to a box furnace for sintering at various temperatures for 10 h.

2.3. Characterization

The phase identification is carried out using a Shimadzu XRD-6000 diffractometer equipped with Fe Kα radiation. The morphology of the samples was examined by a Hitachi S3000N scanning electron microscope (SEM). Energy dispersive spectroscopy (EDS) with EMAX ENERGY EX-250 (HORIBA) was used for composition analysis. Transmission electron microscope (TEM) images were taken using a JEOL JEM-2010 transmission electron microscope. The chemical compositions of the samples sintered at various temperatures were determined using a Perkin Elmer Optima 3000 DC inductively coupled plasma-atomic emission spectrometer (ICP-AES).

2.4. Thermoelectric property measurements

The typical sample shape for electrical resistivity and thermopower is parallelepiped with the dimension of 12.30 × 2.30 × 0.91 mm. Electrical resistivity measurements were performed from room temperature down to liquid nitrogen temperature using the standard four-probe techniques by reversing the current sources to cancel thermoelectric voltages. Temperature-dependent thermopower data were collected between 300 and 80 K using a steady technique. The thermally generated Seebeck voltage across the sample was measured using a Keithley 2182 nanovoltmeter. A type E differential thermocouple was used to measure the temperature difference between the hot and cold ends of the sample, which was measured using Keithley 2000 multimeter. The temperature difference was typically between 0.5 and 1 K. The thermopower of the sample was obtained by subtracting the thermopower of Cu Seebeck probes. Carrier concentration and mobility were determined by Hall measurements using the van der Pauw method under an applied field of 0.55 T (ECOPIA: HMS-3000). Thermal conductivity measurement was carried out using transient plane source techniques with very small temperature perturbations of the sample material by the Hot Disk thermal constants analyzer. The transient plane source technique makes use of a thin sensor element in the shape of a double spiral. The Hot Disk sensor acts both as a heat source for generating temperature gradient in the sample and a resistance thermometer for recording the time dependent temperature increase. The encapsulated sensor is sandwiched between two pieces of samples. During a pre-set time, 200 resistance recordings are taken and from these a relation between temperature and time is established. A few parameters, like the output of power to increase the temperature of the spiral, the measurement time for recording 200 point and the size of the sensor are used to optimize the settings for the measurement. The temperature coefficient of the resistivity (TCR) down to liquid nitrogen temperature for the sensor was determined before measuring

thermal conductivity. The uncertainty for the electrical resistivity, thermopower, and thermal conductivity is about ± 3%, ± 4% and ± 4%, respectively. The sample shape for measuring the temperature dependence of thermal conductivity is rectangular with the dimension of 6.5 mm × 6.5 mm × 4.5 mm.

3. Results and discussion

3.1. Phase identification

Fig. 1 shows the XRD patterns of $Bi_{2-x}Sb_xTe_3$ with $x = 1.5$ and 1.55 which are hydrothermally prepared nanoplatelets and samples after evacuated and encapsulated sintering, respectively. Most of the reflection peaks can be indexed based on a rhombohedra lattice with the space group of $R\bar{3}m$. The (015) and (1010) reflections of the samples have a shoulder on left and right hand side, respectively. Both shoulders belong to (101) and (102) reflections of Te, respectively, indicating the presence of Te.

3.2. SEM and TEM micrographs of $Bi_{2-x}Sb_xTe_3$ with $x = 1.5$ and 1.55

Fig. 2 shows the SEM images of consolidated $Bi_{2-x}Sb_xTe_3$ with $x = 1.5$ and 1.55. There exists porosity in both samples. Fig. 3 shows the TEM images of consolidated $Bi_{2-x}Sb_xTe_3$ with $x = 1.5$ and 1.55. The images clearly show various sizes of nanograins in the microstructure of both samples. Therefore, the consolidated samples can be viewed as nanostructured bulk. The nature of the nanostructured bulk and porosity could play an important role in reducing the lattice thermal conductivity, which will be discussed later.

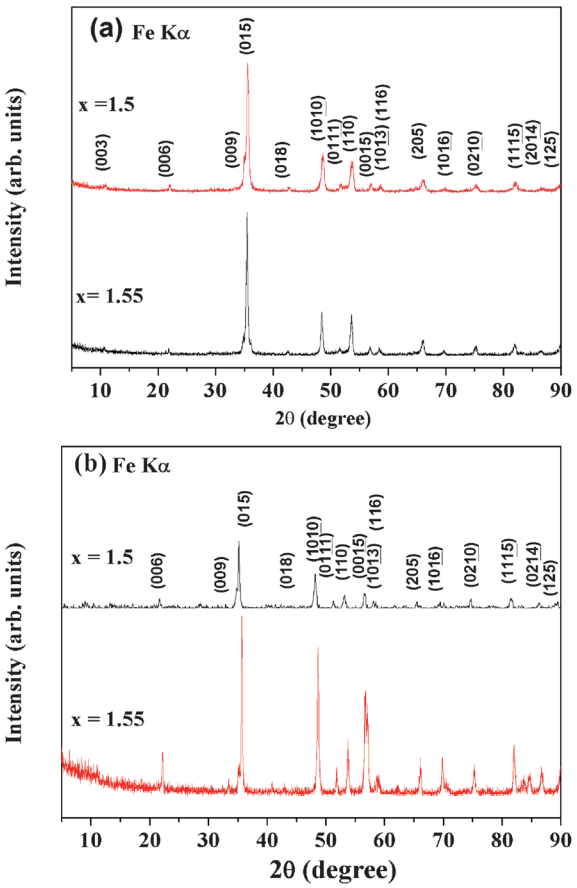

Fig. 1 Powder X-ray diffraction patterns for $Bi_{2-x}Sb_xTe_3$ with $x = 1.5$ and 1.55 which are (a) hydrothermally prepared nanoplatelets and (b) samples after evacuated and encapsulated sintering, respectively.

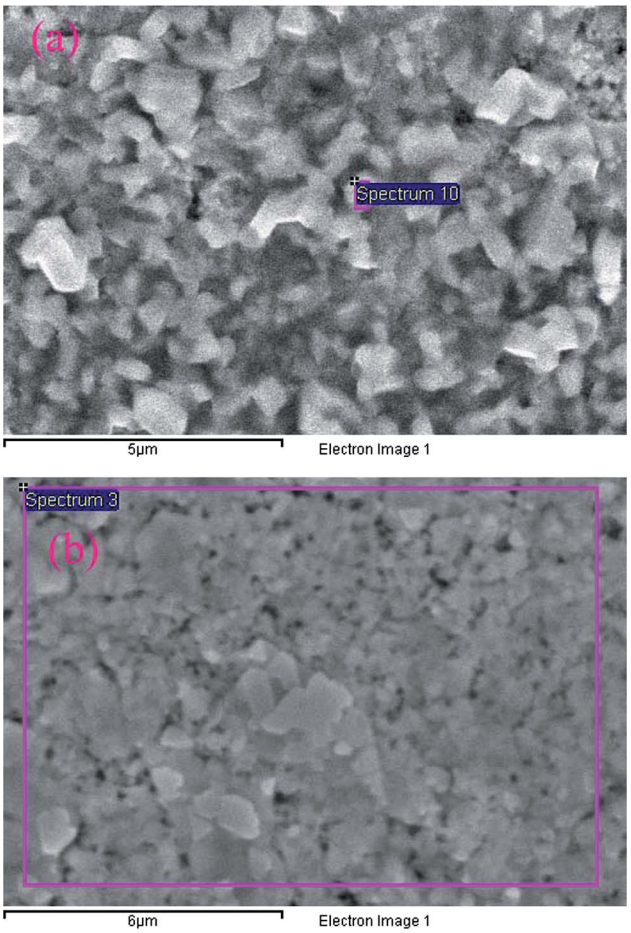

Fig. 2 Scanning electron microscope images for $Bi_{2-x}Sb_xTe_3$ (a) $x = 1.5$ and (b) $x = 1.55$.

3.3. Effect of Sb doping on the electrical conductivity and thermopower

Fig. 4 shows the temperature dependence of electrical conductivity for $Bi_{2-x}Sb_xTe_3$ with $x = 1.45$, 1.5, 1.55 and 1.56, which are

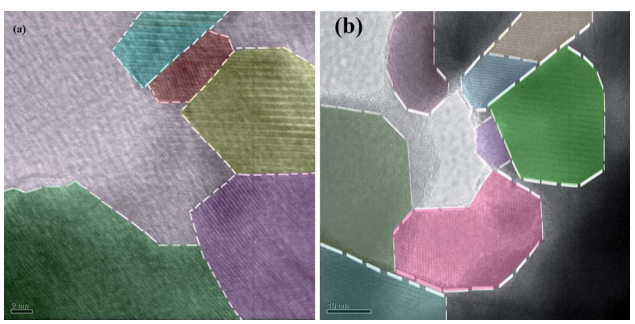

Fig. 3 Transmission electron microscope images showing the nanosized grains for $Bi_{2-x}Sb_xTe_3$ (a) $x = 1.5$ and (b) $x = 1.55$.

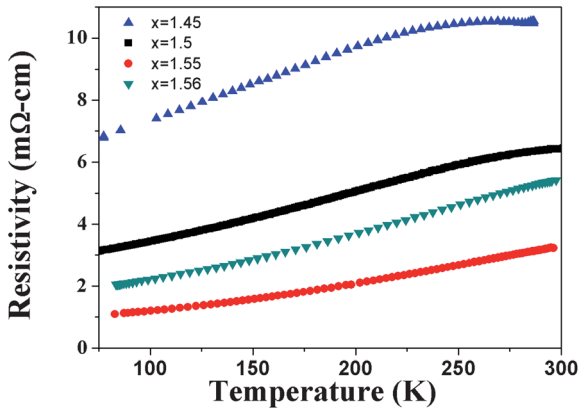

Fig. 4 Temperature dependence of electrical resistivity for compacted $Bi_{2-x}Sb_xTe_3$ with $x = 1.45$, 1.5, 1.55 and 1.56 sintered in an evacuated and encapsulated ampoule.

sintered at 340 °C. It is evident that the $x = 1.55$ sample exhibits the lowest resistivity among these samples. The electrical resistivity at 295 K is 6.42 and 3.24 mΩ cm for $x = 1.5$ and 1.55, respectively. All the samples display metal-like temperature dependence in the investigated temperature range except the $x = 1.45$ sample levelling off at *ca.* 270 K. Using a simple one-carrier and single-band model for calculation in Hall measurements, the room-temperature carrier concentration is 7.31×10^{18} cm^{-3} and 1.05×10^{19} cm^{-3} for $x = 1.5$ and 1.55, respectively. This level of carrier concentration makes the title system a degenerate semiconductor. The metal-like temperature dependence can be attributed to developing an impurity band due to heavy doping in the degenerate semiconductors. The $x = 1.55$ sample shows a significant reduction of electrical resistivity compared to the $x = 1.5$ sample, which is the key factor for the former to enhance the dimensionless figure of merit as compared to the latter one.

Fig. 5 shows the temperature dependence of thermopower for $Bi_{2-x}Sb_xTe_3$ with $x = 1.45$, 1.5, 1.55 and 1.56, which are sintered at 340 °C. The thermopower at 295 K is 273 and 268 μV K^{-1} for $x = 1.5$ and 1.55, respectively. In the low temperature regime the $x = 1.5$ sample exhibits a slightly lower slope and larger size of thermopower than the $x = 1.55$ sample. The slightly smaller size of thermopower corresponds to a larger hole concentration for $x = 1.55$ as compared to $x = 1.5$. This seems to be consistent with the relation between the carrier concentration and thermopower for metals or degenerate semiconductors, which can be expressed as[15,16]

$$s = \frac{8\pi^2 K_B^2}{3eh^2} m^* T \left(\frac{\pi}{3n}\right)^{2/3}, \quad (4)$$

where n is the carrier concentration and m^* is the effective mass of the carrier. It should be noted that the size of thermopower is related to the position of Fermi energy.[17] Although the Fermi energy depends on the Sb content, it varies only slightly in the range of $x = 1.4$ and 1.6.[18] Fig. 6 shows the temperature dependence of power factor σS^2 for $Bi_{2-x}Sb_xTe_3$ with = 1.45, 1.5, 1.55 and 1.56, which are sintered at 340 °C. The power factor at 290 K is 11.9 μW cm^{-1} K^{-2} and 23.4 μW cm^{-1} K^{-2} for $Bi_{2-x}Sb_xTe_3$ with $x = 1.5$ and 1.55, respectively. The enhanced power factor of the $x = 1.55$ sample can be readily seen and can be ascribed to its increased electrical conductivity. Fig. 7 shows the temperature dependence of both resistivity and thermopower for the samples with $x = 1.55$ which were synthesized and sintered in different batches. The results show that the data of both resistivity and thermopower can be reproduced.

3.4. Effect of sintering temperature on the electrical conductivity and thermopower

It is known that processing temperature has an effect on the composition and carrier concentration of p-type $Bi_{2-x}Sb_xTe_3$ due to the volatility of Te, which causes the Te-deficiency in the stoichiometry.[19,20] Since the hydrothermally synthesized $Bi_{2-x}Sb_xTe_3$ nanopowders can be consolidated at low temperatures, the transport behavior of encapsulated and sintered $Bi_{2-x}Sb_xTe_3$ would be different from those fabricated using different techniques. Table 1 summarizes the chemical compositions obtained by the analyses using inductively coupled plasma atomic emission spectroscopy (ICP-AES) for the samples of $x = 1.5$ sintered at various temperatures. Table 2 summarizes the chemical compositions obtained by EDS in 7 different spots for the $x = 1.55$ sample. Therefore, it would be

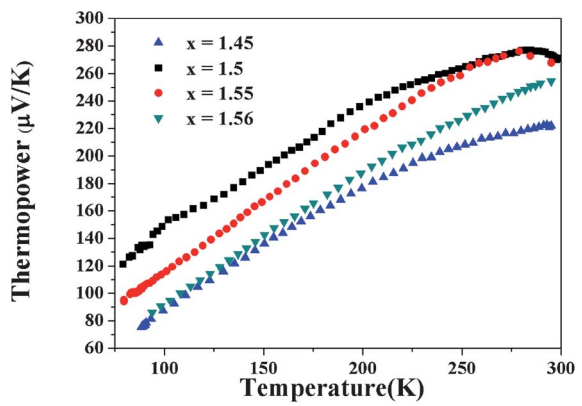

Fig. 5 Temperature dependence of thermopower for compacted $Bi_{2-x}Sb_xTe_3$ with $x = 1.45$, 1.5, 1.55 and 1.56 sintered in an evacuated and encapsulated ampoule.

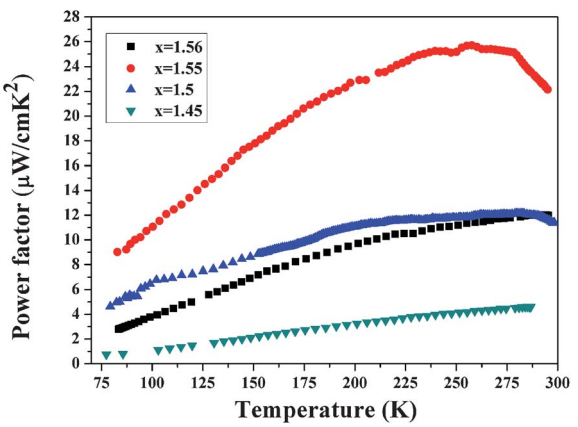

Fig. 6 Temperature dependence of power factor for compacted $Bi_{2-x}Sb_xTe_3$ with $x = 1.45$, 1.5, 1.55 and 1.56 sintered in an evacuated and encapsulated ampoule.

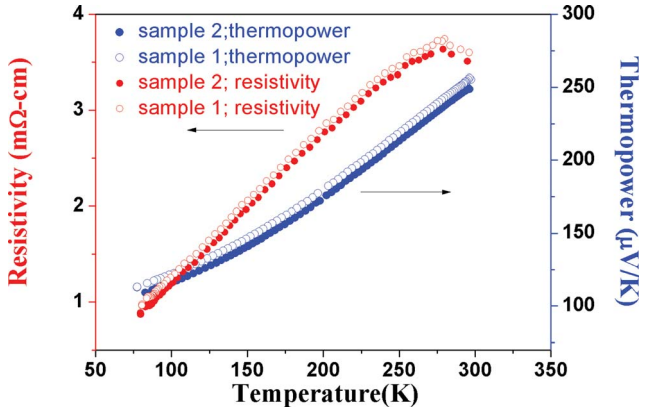

Fig. 7 Temperature dependence of both resistivity and thermopower for two samples of compacted $Bi_{2-x}Sb_xTe_3$ with nominal $x = 1.55$ synthesized in different batches.

Table 1 Chemical analysis by ICP-AES for $(Bi,Sb)_2Te_{3-\delta}$ with nominal $x = 1.55$ obtained by sintering in an evacuated and encapsulated ampoule at various temperatures

	Bi (wt%)	Sb (wt%)	Te (wt%)	Bi	Sb	Te	δ
300 °C	13.3	28.7	52.2	0.42	1.58	2.74	0.26
320 °C	13.6	30.0	53.7	0.42	1.58	2.70	0.30
340 °C	13.5	30.0	54.6	0.42	1.58	2.75	0.25
360 °C	13.9	30.0	54.0	0.42	1.58	2.69	0.31
380 °C	14.0	30.2	53.8	0.42	1.58	2.67	0.33

necessary to investigate the effects of sintering temperature on the transport properties of $Bi_{2-x}Sb_xTe_3$ consolidated by encapsulating-and-sintering techniques. Figs. 8 and 9 show the temperature dependence of electrical conductivity and thermopower for $Bi_{0.45}Sb_{1.55}Te_3$ sintered at various temperatures between 300 °C and 380 °C. It is evident that the sintering temperature plays a role on the size of electrical resistivity and thermopower. As shown in Fig. 10, the carrier concentration and mobility vary with the sintering temperature. Higher processing temperatures would be expected to have a larger degree of Te-deficiency.[21] Nevertheless, the carrier concentration does not seem to correlate well with the expected tendency (Table 1 and Fig. 10). Materials with higher carrier concentration would be expected to have smaller thermopower according to eqn (4). However, the relation between thermopower and carrier concentration shown in Fig. 11 dose not follow the tendency expected from eqn (4). This situation might arise from the

Table 2 Chemical analysis by EDS for $(Bi,Sb)_2Te_{3-\delta}$ with nominal $x = 1.55$ obtained by sintering in an evacuated and encapsulated ampoule

Bi (wt%)	Sb (wt%)	Te (wt%)	Bi	Sb	Te
15.78	31.87	52.35	0.45	1.55	2.43
15.21	31.09	53.70	0.44	1.56	2.56
16.01	31.89	52.10	0.45	1.55	2.45
16.03	31.10	52.88	0.46	1.54	2.49
16.49	30.51	53.00	0.47	1.53	2.52
15.31	31.74	52.95	0.44	1.56	2.48
15.32	31.10	53.58	0.45	1.55	2.54

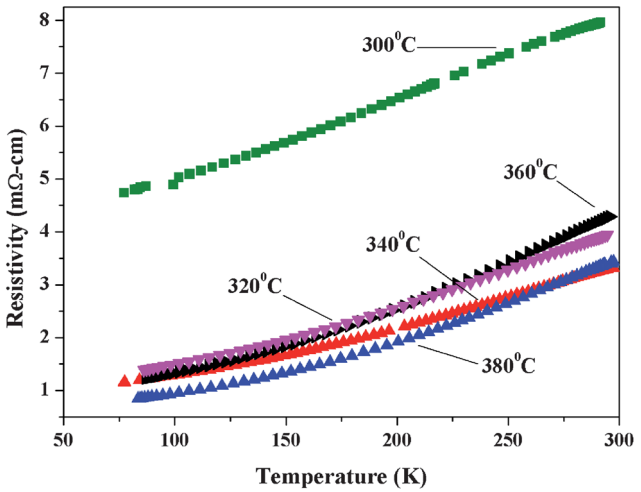

Fig. 8 Temperature dependence of electrical resistivity for compacted $Bi_{0.45}Sb_{1.55}Te_3$ sintered at different temperatures of 300–380 °C in an evacuated and encapsulated ampoule.

mixed conduction due to simultaneous contributions from allowed states in the valence band and antisite defects. The electron carriers from the valence band would contribute negative values to the total thermopower, whereas the hole carriers from antisite defects contribute positive values to the total thermopower. Therefore, in order to optimize the power factor, searching for appropriate sintering temperature for different fabrication procedures is necessary. Fig. 12 shows the temperature dependence of power factor for $Bi_{0.45}Sb_{1.55}Te_3$ sintered at various temperatures between 300 °C and 380 °C. The sample sintered at 340 °C shows the largest power factor among the samples above 170 K.

3.5. Thermal conductivity of $Bi_{2-x}Sb_xTe_3$ with $x = 1.5$ and 1.55

The $x = 1.5$ and 1.55 samples represent the best two power factors in this study, therefore, thermal conductivity

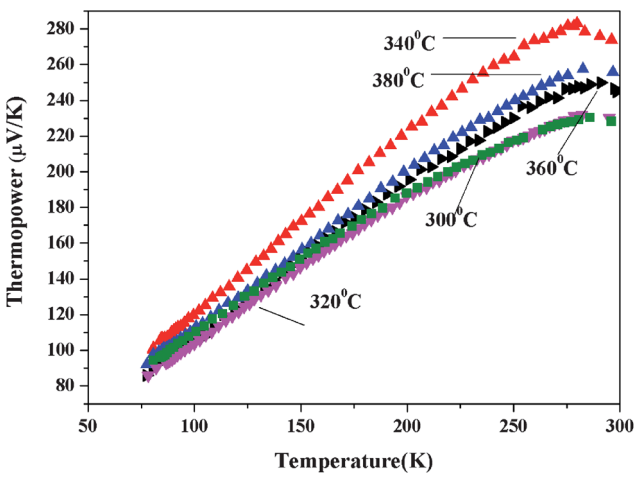

Fig. 9 Temperature dependence of thermopower for compacted $Bi_{0.45}Sb_{1.55}Te_3$ sintered at different temperatures of 300–380 °C in an evacuated and encapsulated ampoule.

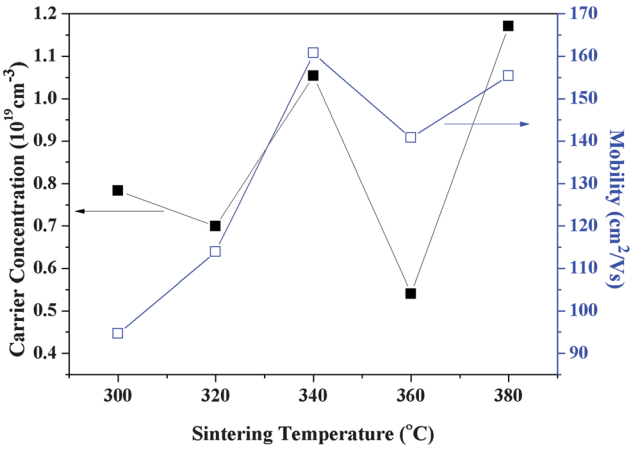

Fig. 10 Carrier concentration and mobility at room temperature for compacted $Bi_{0.45}Sb_{1.55}Te_3$ sintered at different temperatures of 300–380 °C in an evacuated and encapsulated ampoule.

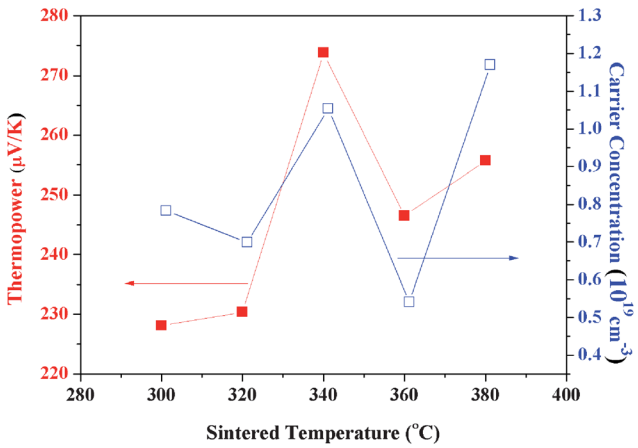

Fig. 11 Thermopower and carrier concentration at room temperature for compacted $Bi_{0.45}Sb_{1.55}Te_3$ sintered at different temperatures of 300–380 °C in an evacuated and encapsulated ampoule.

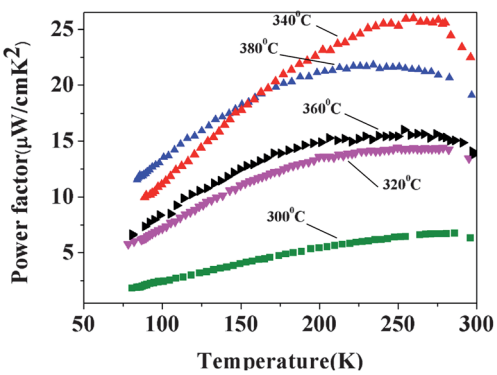

Fig. 12 Temperature dependence of power factor for compacted $Bi_{0.45}Sb_{1.55}Te_3$ sintered at different temperatures of 300–380 °C in an evacuated and encapsulated ampoule.

measurements are carried out only for these two samples. Thermal conductivity of a solid consists of a component arising from the electronic charge carriers and a component arising from the lattice, that is, $\kappa = \kappa_{el} + \kappa_L$, where κ_{el} and κ_L represent the electronic and lattice thermal conductivity, respectively. The Wiedemann-Franz law, which may be used to estimate κ_{el} from electrical conductivity, is expressed by

$$\frac{\kappa_{el}}{\sigma} = \frac{\pi^2}{3}\left(\frac{k_B}{e}\right)^2 T = L_0 T, \quad (5)$$

where L_0 is the Lorenz number and has the size of 2.45×10^{-8} WΩ K^{-2} for a degenerate semiconductor. According to eqn (5), increasing the electrical conductivity σ will simultaneously increase κ_{el}. This would sabotage the advantage of increasing the electrical conductivity in attempting to enhance the ZT values. According to Holland's model,[22] the lattice thermal conductivity can be described as follows:

$$\kappa_L = \frac{1}{3} v_g \int_0^{\theta_D/T} c_V \tau d\left(\frac{\hbar\omega}{k_B T}\right), \quad (6)$$

where θ_D is the Debye temperature, v_g is the velocity of phonons, τ is the relaxation time, and ω is the phonon angular frequency. Assuming the phonon spectrum is not altered, the thermal conductivity would be primarily associated with τ in the phonon scattering processes. Reduction of τ could arise from combined processes such as Umklapp scattering, phonon-defect scattering, or phonon–grain boundary scattering.[23] For the phonon–grain boundary scattering, the size of τ depends on the average grains size, which can be formulated as[24]

$$\frac{1}{\tau_{grain}} = \frac{v_g}{d}\left(\frac{1-p(\omega)}{1+p(\omega)}\right), \quad (7)$$

where $p(\omega)$ is the probability of specular reflection and d is the average grain size. In all the p-type $Bi_{2-x}Sb_xTe_3$ nanostructured bulk prepared by various methods,[4–6] a significant reduction of lattice thermal conductivity has been observed, which in turn leads to considerable enhancement of ZT. In a study of inelastic neutron scattering experiments, it is found that generalized phonon density of states for $Bi_{2-x}Sb_xTe_3$ obtained by zone melting and melt-spinning/spark-plasma-sintering procedures are virtually identical.[25] This study may indicate that a strong scattering of phonons by nanograins has occurred since a drastically altered phonon spectrum is not observed in the nanostructured bulk. Fig. 13 shows the temperature dependence of thermal conductivity for $Bi_{2-x}Sb_xTe_3$ with x = 1.5 and 1.55. The thermal conductivities are 0.36 Wm^{-1}K^{-1} at 297 K for x = 1.5 and 0.41 Wm^{-1}K^{-1} at 290 K for x = 1.55. According to eqn (5), the calculated electronic thermal conductivities κ_{el} for x = 1.5 are 0.11 Wm^{-1}K^{-1} at 297 K and 0.22 Wm^{-1}K^{-1} at 290 K for x = 1.55. Therefore the lattice thermal conductivity κ_L would be 0.25 Wm^{-1}K^{-1} at 297 K for x = 1.5 and 0.19 Wm^{-1} K^{-1} at 290 K for x = 1.55. The thermal conductivities of our samples are remarkably low, which can be ascribed to the small sizes of electronic and lattice contributions. The small size of κ_{el} is associated with its low electrical conductivity as compared to similar compositions of $Bi_{2-x}Sb_xTe_3$. The small size of κ_L could be associated with the nanograins in our materials. As shown in Fig. 3, the various

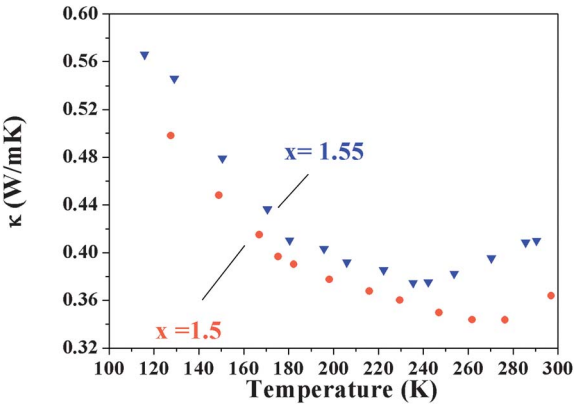

Fig. 13 Temperature dependence of thermal conductivity for compacted $Bi_{2-x}Sb_xTe_3$ with $x = 1.5$ and 1.55 sintered in an evacuated and encapsulated ampoule.

sizes of nanograins may play a significant role in effectively scattering different phonon modes.[26] The lattice thermal conductivity at room temperature of our sample is as low as that of the sample obtained from melt spinning/spark plasma sintering procedure.[5,25]

According to eqn (6) and (7), a small average size of these nanosized grains would lead to a small κ_L. Besides, since the density of compacted and sintered sample is less than 90% of its theoretical density, the porous microstructure may be expected. Porosity would lead to further reduction of thermal conductivity.[23] Therefore, the small observed κ_L could be mainly attributed to the nanosized grains and porosity of the sample. The maximum dimensionless thermoelectric figure of merit ZT shown in Fig. 14 is 0.97 at 276 K for $x = 1.5$, and 1.75 at 270 K for $x = 1.55$. The ZT value of 1.65 at 290 K is about a 65% increase of commercial ingots.

4. Conclusion

In summary, p-type $Bi_{2-x}Sb_xTe_3$ with $x = 1.5$ and 1.55 are fabricated by hydrothermal methods followed by a sintering procedure in an evacuated ampoule. We have shown that the $x = 1.55$ sample exhibits a state-of-the-art dimensionless figure of merit $ZT = 1.65$ at 290 K and 1.75 at 270 K with significant improvement of that for the commercial Bi_2Te_3 materials because of low thermal conductivity and the decrease of resistivity.

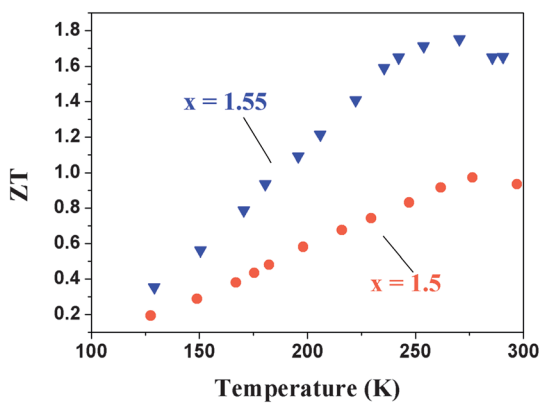

Fig. 14 Temperature dependence of dimensionless figure of merit for compacted $Bi_{2-x}Sb_xTe_3$ with $x = 1.5$ and 1.55 sintered in an evacuated and encapsulated ampoule.

Acknowledgements

This work is supported by the National Science Council of Taiwan, ROC, grant No. NSC 98-2112-M-018-005-MY3.

References

1 Oak Ridge Leadership Computing Facility Snapshot, The Week of January 25, 2010.
2 G. A. Slack, in *CRC Handbook of Thermoelectrics* (Ed: D. M. Rowe), CRC Press, Boca Raton, FL 1995.
3 A. J. Minnich, M. S. Dresselhaus, Z. Ren and G. Chen, *Energy Environ. Sci.*, 2009, 466–479.
4 B. Poudel, Q. Hao, Y. Ma, Y. Lan, A. Minnich, B. Yu, X. Yan, D. Wang, A. Muto, D. Vashaee, X. Chen, J. Liu, M. S. Dresselhaus, G. Chen and Z. Ren, *Science*, 2008, **320**, 634–638.
5 W. Xie, X. Tang, Y. Yan, Q. Zhang and T. M. Tritt, *Appl. Phys. Lett.*, 2009, **94**, 102111–102113.
6 S. Fan, J. Zhao, J. Guo, Q. Yan, J. Ma and Huey Hoon Hng, *Appl. Phys. Lett.*, 2010, **96**, 182104–182106.
7 X. B. Zhao, X. H. Ji, Y. H. Zhang, T. J. Zhu, J. P. Tu and X. B. Zhang, *Appl. Phys. Lett.*, 2005, **86**, 062111–062113.
8 W. Lu, Y. Ding, Y. Chen, Z. L. Wang, J. Fang and J. Am, *J. Am. Chem. Soc.*, 2005, **127**, 10112–10116.
9 Y. Deng, C. W. Cui, N.-L. Zhang, T. H. Ji, Q. Yang and L. L. Guo, *Solid State Commun.*, 2006, **138**, 111–113.
10 C.-J. Liu, G.-J. Liu, C.-W. Tsao, Y.-F. Lu, L.-S. Chang, *Proceedings of 26th, International Conference on Thermoelectrics* 2007, p.30-p.33.
11 C.-J. Liu, G.-J. Liu, Y.-L. Liu and L.-R. Chen, *J. Mater. Res.*, 2011, **26**, 1755–1761.
12 Z. Starý, J. Horák, M. Stordeur, M. Stölzer and J. Phys, *J. Phys. Chem. Solids*, 1988, **49**, 29–34.
13 X. A. Fan, J. Y. Yang, W. Zhu, S. Q. Bao, X. K. Duan, C. J. Xiao, Q. Q. Zhang and Z. Xie, *Appl. Phys.*, 2006, **39**, 5069–5073.
14 C.-J. Liu, G.-J. Liu, C.-W. Tsao, Y.-J. Huang and J. Electron, *Mater*, 2009, **38**, 1499–1503.
15 Y. Zhao, J. S. Dyck, B. M. Hernandez, C. Burda and J. Am, *J. Am. Chem. Soc.*, 2010, **132**, 4982–4983.
16 M. Cutler, J. F. Leavy and R. L. Fitzpatrick, *Phys. Rev.*, 1964, **133**, A1143–A1152.
17 G. J. Snyder and E. S. Toberer, *Nat. Mater.*, 2008, **7**, 105–114.
18 G. S. Nolas, J. Sharp, and H. J. Goldsmid, *Thermoelectrics: Basic Principles, and New Materials Developments*, Springer, Berlin, 2001, p. 38.
19 M. Stordeur, in *CRC Handbook of Thermoelectrics* (Ed: D. M. Rowe), CRC Press, Boca Raton, FL 1995, p. 251.
20 C.-W. Hwang, D.-B. Hyun, H.-P. Ha, T. S. Oh and J. Mater, *Sci*, 2001, **36**, 3291–3297.
21 H. Scherrer and S. Scherrer, in *CRC Handbook of Thermoelectrics* (Ed: D. M. Rowe), CRC Press, Boca Raton, FL 1995, p. 226.
22 M. G. Holland, *Phys. Rev.*, 1963, **132**, 2461–2471.
23 P. E. Hopkins, P. T. Rakich, R. H. Olsson, I. F. El-kady and L. M. Phinney, *Appl. Phys. Lett.*, 2009, **95**, 161902–161904.
24 J. E. Graebner, M. E. Reiss and L. Seibles, *Phys. Rev. B: Condens. Matter*, 1994, **50**, 3702–3713.
25 W. Xie, J. He, H. J. Kang, X. Tang, S. Zhu, M. Laver, S. Wang, J. R. D. Copley, C. M. Brown, Q. Zhang and T. M. Tritt, *Nano Lett.*, 2010, **10**, 3283–3289.
26 C. J. Vineis, A. Shakouri, A. Majumdar and M. G. Kanatzidis, *Adv. Mater.*, 2010, **22**, 3970–3980.